CrystEngComm

Accepted Manuscript

ROYAL SOCIETY OF CHEMISTRY

www.rsc.org/crystengcomm

Regulated morphology/phase structure and enhanced fluorescence in YF_3: Eu^{3+}, Bi^{3+} via a facile method

Fengying Lei,[a] Xiao Zou,[a] Na Jiang,[a] Qiaoji Zheng,[a] Kwok Ho Lam,[b] Lingling Luo,[a] Zhanglei Ning[a] and Dunmin Lin[a*]

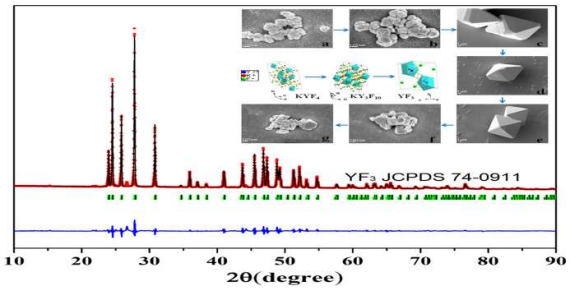

Using a handily method to regulate morphology/phase structure and significantly enhance fluorescence in YF_3: Eu^{3+}, Bi^{3+}.

Regulated morphology/phase structure and enhanced fluorescence in YF_3: Eu^{3+}, Bi^{3+} via a facile method

Fengying Lei[a], Xiao Zou[a], Na Jiang[a], Qiaoji Zheng[a], Kwok Ho Lam[b], Lingling Luo[a], Zhanglei Ning[a] and Dunmin Lin[a,*]

[a] College of Chemistry and Materials Science, Sichuan Normal University, Chengdu 610066, P. R. China. *Corresponding author: Tel. +86 28 84760802; fax. +86 28 84767868; E-mail ddmd222@sicnu.edu.cn

[b] Department of Electrical Engineering, The Hong Kong Polytechnic University, Kowloon 999077, Hong Kong, P.R China

Abstract

A simple and facile hydrothermal method has been developed to enhance the fluorescence performance of YF_3: xEu^{3+}, $y\%Bi^{3+}$ (x = 0-0.2, y = 0-1.5) via optimizing the concentration of Eu^{3+} and Bi^{3+} and regulating the morphology/phase structure by controlling the amount of HNO_3. The evolutionary mechanism of the micro-topography and microstructure for the samples has been proposed, and the fluorescence and decay properties of the samples have been investigated. It was found that the fluorescence intensity of the sample has been enhanced greatly after added the opportune amount of Bi^{3+}. The optimum concentrations of Eu^{3+} and Bi^{3+} for fluorescence are x = 0.125 and y = 0.5%, respectively. The significant enhancement in fluorescence performance could be obtained in the sample with the desired morphology at the optimum volume of HNO_3 (V_{HNO_3} = 11 mL).

Introduction

In recent years, lanthanide ions doped inorganic crystals with controllable shapes and sizes have attracted considerable attention because of their potential technological applications in biomedical imaging, anti-fake label and illumination.[1] Among these inorganic materials, fluoride-containing host materials are the most captivating due to their low vibration energy, minimization of the quenching of the correlative excited state of the rare-earth ions and good optical transparency at a wide wavelength region.[2,3] Meanwhile, fluoride-containing materials possess good solubility, adequate thermal and environmental stabilities. These excellent physicochemical properties are in favor of the optical applications of the materials.[4] In comparison with other fluorescent host materials, YF_3 is considered as one of the most important host materials that has been intensively studied in recent years.[5,6] It has been known that trivalent rare earth ions can easily substitute for Y^{3+} in the YF_3 because of their similar ionic radii of lanthanide. Moreover, the consummate matrix of YF_3 is conducive to lanthanides doping thus promoting the high efficiency emission of down/up conversion materials without additional charge compensation.[5,7]

Among rare earth ions, Eu^{3+} has been frequently used as an activator due to its intense emission caused by $^5D_0 \rightarrow {}^7F_2$ transition in red spectral region. A number of investigations have been carried out to improve the fluorescence efficiency of Eu-containing materials by doping metal ions (*e.g.* Ln^{3+}-doped calcium fluoride nanocrystals, $NaxEu^{3+}_{(2-x)/3}MoO_4$, *etc.*),[4,8,9] employing various synthesis techniques (e.g. a facile arginine-assisted hydrothermal synthesis, electrospinning, *etc.*)[10,11] and optimizing the stoichiometric ratio of the materials (*e.g.* $Eu_{1-x}Bi_xVO_4$, $BaLa_{2-x-y}ZnO_5$: xBi^{3+},yEu^{3+}, *etc.*).[12,13] Eu^{3+} has also been introduced into YF_3 to obtain laser materials with excellent emission. For example, Shao *et al*. studied YF_3: Eu^{3+} micro-single crystals,[7] and Fu *et al*. fabricated Eu^{3+}-doped YF_3 microcrystals with uniform grains.[14] These studies control the morphology of crystal grains to improve the fluorescence performance of the material by adding

different inorganic salts. On the other hand, it has been noted that the energy can be transferred from Bi^{3+} to Eu^{3+} via a dipole-dipole mechanism in $ZnWO_4$: Bi^{3+},Eu^{3+} materials.[15] Thus, Bi^{3+} has been considered as a significant luminescent sensitizer for Eu^{3+}. Recently, Dong *et al*.[13] and Wang *et al*.[15] have obtained the $ZnWO_4$: Bi^{3+},Eu^{3+} material with excellent luminescence induced by the energy transferring from Bi^{3+} to Eu^{3+}. Therefore, it can be reasonably anticipated that the introduction of Bi^{3+} into the YF_3: Eu^{3+} materials may effectively improve the fluorescence of the materials. To our knowledge, there have been few reports on Bi^{3+} sensitized Eu^{3+} in YF_3 host material. In addition, it is well known that the morphology and crystal structure of crystalline grains usually dominate the properties of materials.[16] In general, the morphology and phase structure of nano/micromaterials depend on many factors (*e.g*. the variety and concentration of solvent, the types and levels of doping ions, reaction time and temperature, *etc*.).[17] Some studies have revealed that the technology application of most materials depends on the characteristic dimension.[18] Generally, the morphology control of crystal grain is crucial to offset the disadvantage and optimize the performance of the materials.[19] As well known, the morphologies of grains essentially depend on the growth rate of crystal facets and the stability of surfaces. Thus, various phases and morphologies of the materials always can be modulated via different synthetic methods. For instance, a hexagonal YF_3 was obtained via a micro-emulsion;[20] a hollow nano-fibers of YF_3 was synthesized by an double-crucible method;[11] and various solvents (*e.g*. ethylenediamine tetraacetic acid disodium salt, polyethylenimine polymer, *etc*.)[21,22] were also introduced to obtain the materials with desired morphologies.[2]

Unfortunately, the operations mentioned above are difficult to control. Besides, some additional impurities or defects are usually produced in desired materials. To overcome these difficulties, it is necessary to develop a simple technology for controlling the micro-topography of crystal particles

to enhance the material properties. It has been noted that the morphology of microscopic particles strongly depends on the concentration of H^+ ions and inorganic doping, [7, 14] because the energy that applied on the grains is determined by the kinetics of the ions in the reaction system. As a result, changing the concentration of H^+ ion may be an effective method to simply regulate the morphology of grains. In the present work, new materials of YF_3: xEu^{3+}, $y\%Bi^{3+}$ have been developed by adding Bi^{3+} to YF_3: Eu^{3+} with a simple facile hydrothermal process. The grain morphology/phase structure has been successfully regulated only by modulating the HNO_3 level, and a significant enhancement in the fluorescence of the materials has been obtained. The dependences of fluorescence and decay properties on the morphology have also been studied in detail.

Experimental Sections

Materials synthesis: The powders of YF_3: xEu^{3+}, $y\%Bi^{3+}$ (x = 0-0.2, y = 0-1.5) were synthesized by a facile hydrothermal route. All chemicals were purchased from Sinopharm Chemical Reagent Co., Ltd (China) and directly used without any treatment. In a typical synthesis, Eu_2O_3 (99.99%), Y_2O_3 (99.99%), Bi_2O_3 (99.999%) in stoichiometric ratio of the YF_3: xEu^{3+}, $y\%Bi^{3+}$ were dissolved in 65% HNO_3 (5-17 mL) and magnetic stirred at 60^{o}C for 40 min. $KF{\cdot}2H_2O$ (99%) and Y^{3+} with a molar ratio of 6:1 was dissolved in distilled water, and then the resulting fluorine-containing solution was added dropwise to the solution containing rare earth ions under vigorous stirring and the resultant bulk volume was fixed at 30mL. The mixture was transferred into 100mL Teflon-line autoclave and heated at 200^{o}C for 18 h in a muffle furnace. When the autoclave was cooled to room temperature, the white products were collected via centrifuging and washing several times with distilled water and ethanol, and finally dried at 80^{o}C in air for 12 h.

Instrumentation: The crystal structures of the powder were examined using X-ray diffraction (XRD) with Cu Kα radiation (Smart Lab). The microstructures (SEM) were observed by a field-emission scanning electron microscope (FE-SEM,JSM-7500, Japan). The fluorescent spectral information was recorded by using a fluorescence spectrophotometer (F-7000) with a xenon lamp. The internal and external quantum efficiency QE were measured using a QE-2100 from Otsuka Photal Electronics. Transmission electron microscopy (TEM) and high-resolution (HRTEM) were performed on a JEM2010.

Results and discussions

The XRD patterns of the YF_3: xEu^{3+}, 1.0%Bi^{3+} powders prepared at V_{HNO_3} = 11mL are shown in Fig. 1. The sample without Eu^{3+} doping is mainly the mixture of hexagonal KYF_4 (JCPDS No. 27-0466) and tetragonal KY_3F_{10} (JCPDS No. 27-0465). In addition, a small amount of YF_3 (JCPDS No. 74-0911) is observed in the sample with x = 0. It can be seen that Eu^{3+} doping leads to an obvious change in the crystal structure of the samples. As x increases, the observed numbers of KY_3F_{10} and KYF_4 peaks reduce gradually while the number of YF_3 peaks increases. At $x \geq 0.075$, all the samples consist of pure YF_3 with orthorhombic symmetry and no other impurities can be detected. For the materials with $x \geq 0.075$, the further increment in the doping level of Eu^{3+} does not cause the change in the phase structure of the samples. At low levels of Eu^{3+}, the main factor that determines the phase structure of the samples should be the concentration of hydrogen bonds (H···O) in the materials, which will be discussed in the following paragraph.

Fig. 2 shows the EDS spectra of YF_3: xEu^{3+}, 1.0%Bi^{3+} samples with x = 0, 0.05, 0.10 and 0.15 and the insets show the atomic percentages of the elements and corresponding micro-morphologies. It can be seen that as x (*i.e.* the content of Eu^{3+}) increases from 0 to 0.15, the concentration of

oxygen increases from 0 to 2.49% that is in favor of the H···O bond formation. On the basis of the transition state theory,[23] the formation of H···O bond plays a role of bridge in the formation of fluorine hydrogen bond (F···H). Since the bonding energy of the H···O bond is weaker than that of the F···H bond, the latter possesses more preferable stability. Therefore, most of the H^+ ions combine with excess F^{-1} to crystallize into stable YF_3 phase at the presence of sufficient oxygen. At low levels of Eu^{3+} ($x < 0.075$), the low concentration of oxygen results in the insufficient concentration of H···O bond that is not favor in the formation of F···H bond, so that the excess F^- ions are mainly formed to multiple-fluoride (KYF_4, KY_3F_{10}). At $x = 0.075$, the equilibrium of the transition from H···O to H···F may be reached, resulting in the pure YF_3. When Eu^{3+} is excess ($x > 0.075$), the phase structure of the samples has not been changed with further increasing x because of a preferable stability of the YF_3.[7]

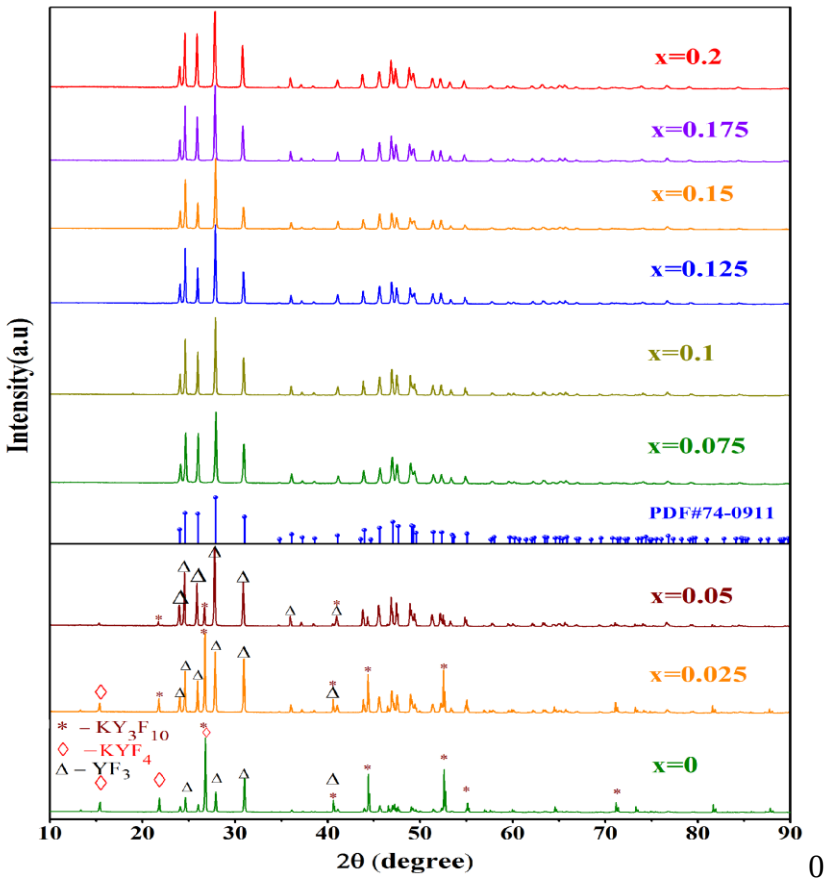

Fig. 1 XRD patterns of YF_3: xEu^{3+}, 1.0%Bi^{3+} samples (x = 0-0.2) prepared at V_{HNO_3} = 11mL.

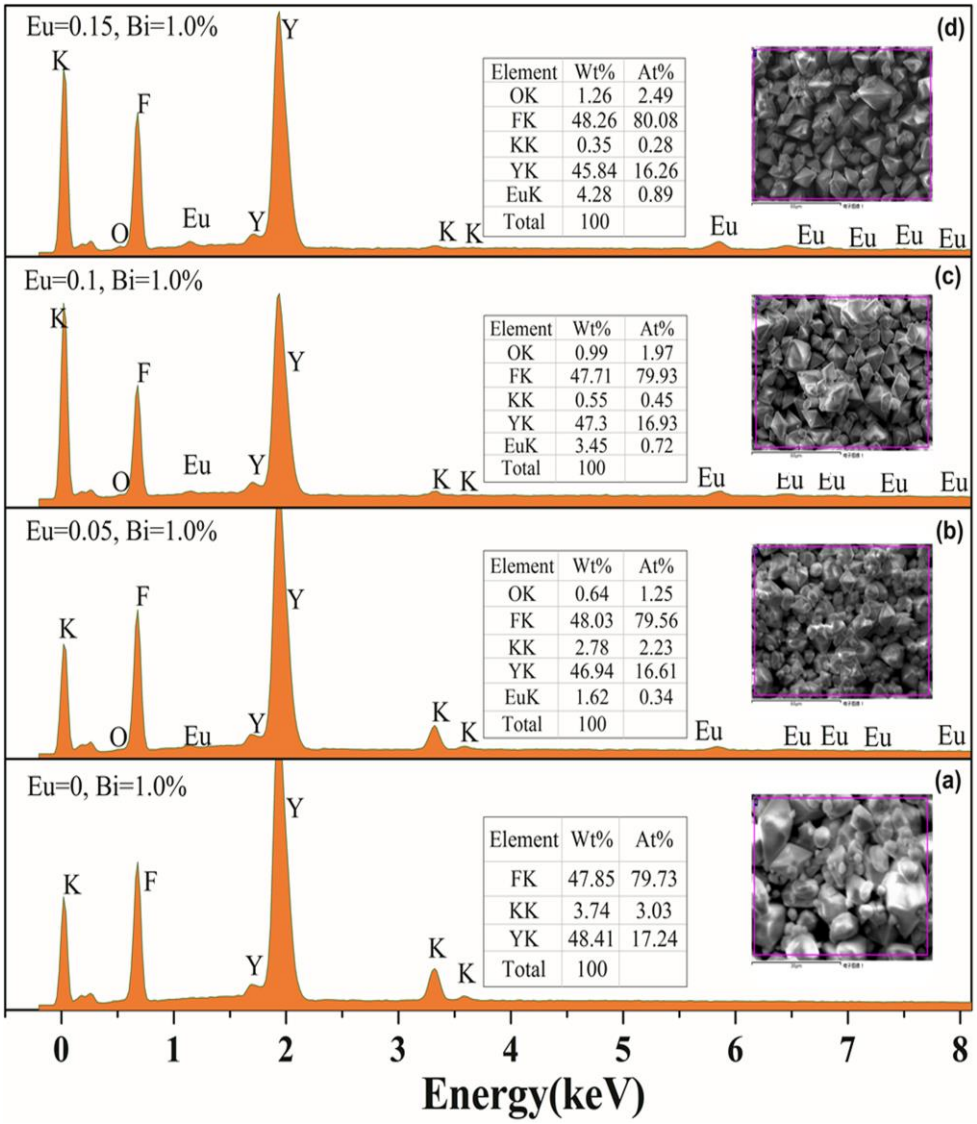

Fig. 2 EDS spectra of YF_3: xEu^{3+}, 1.0%Bi^{3+} samples with x = 0, 0.05, 0.10 and 0.15 prepared at V_{HNO_3} = 11mL. The insets show the atomic and weight percentages of the elements and corresponding surface morphologies.

Fig. 3 shows the SEM micrographs of the YF_3: xEu^{3+}, 1.0%Bi^{3+} samples with x = 0, 0.025, 0.05, 0.10, 0.125, 0.15 and 0.175. It can be clearly seen that Eu^{3+} doping leads to a distinct change in the micro-topography of the samples. From Fig. 3a, the sample with x = 0 exhibits irregular multipolygon spherical particles with rough surface and nonuniform grain size. Some pores and defects can also be observed. With x increasing from 0.025 to 0.075, the surface of the grains becomes relatively smooth, and some octahedral and irregular octahedral morphologies are

simultaneously observed. For the sample with x = 0.10, the surface and size of the grains are very smooth and relatively uniform such that the grains mainly possess diamond-like morphology and perfect octahedron, and there is no obvious flaw on the surface of the grains. However, excess Eu^{3+} destroys the perfection of the grains. It can be seen that with x further increasing from 0.10 to 0.175, the grains become irregular and nonuniform. Some bigger octahedra and irregular truncated octahedra like kernel and small crystals aggregated on the surface of the grains are observed in Figs. 3f-h, indicating that the aggregated particles may be formed by a new complex geometrical structure and the small particles may be served as building blocks for forming smaller nano-octahedra.[21] On the basis of the Ostwald ripening process,[24] the truncated octahedral particles formed earlier would act as a seed of YF_3 grain on which other small orthorhombic YF_3 become large ideal truncated octahedra eventually. In addition, the average size of the grains first increases and then decreases with x increasing.

Figs. 4 and 5 show the XRD patterns and SEM micrographs of the YF_3: $0.125Eu^{3+}$, $y\%Bi^{3+}$ samples with y = 0, 0.5, 1.0, and 1.5 prepared at V_{HNO_3} = 11 mL, respectively. At $y \leq 1.0$, all the diffraction peaks of the powders are identical with the standard card (JCPDS 74-0911) for orthorhombic YF_3, indicating that the samples possess pure orthorhombic phase without impurities after the moderate Bi^{3+} doping. This suggests that Bi^{3+} ions are incorporated in the lattice of host material with little influence on the lattice matrix due to the comparable ionic radius of Bi^{3+} with Y^{3+} and Eu^{3+}.[25] However, an impurity phase of KY_3F_{10} is observed with y increasing to 1.5. Meanwhile, from Fig. 5, the microstructure of the samples is significantly changed with increasing y. The grain size of the materials first increases and then diminishes with increasing the amount of Bi^{3+}. At y = 0, small crystal grains of the samples aggregate on the large grains. With the addition of $0.5\%Bi^{3+}$, the relative regular and monodispersed octahedra are obtained. When Bi^{3+} is excess ($y \geq$

1.0), the crystal grains become irregular and agglomerate. After the addition of Bi^{3+}, the growth rate of different crystalline planes is changed because the Bi^{3+} ions are selectively absorbed on the surface of the initially formed tiny YF_3 crystals; meanwhile, the existing anions (F^-, OH^- and NO_3^-) are coordinated by different coordination strengths and modes.[14] These lead to the change in the grain shape of YF_3 materials. On the other hand, the charge of cations may also be responsible for the size of YF_3.[14]

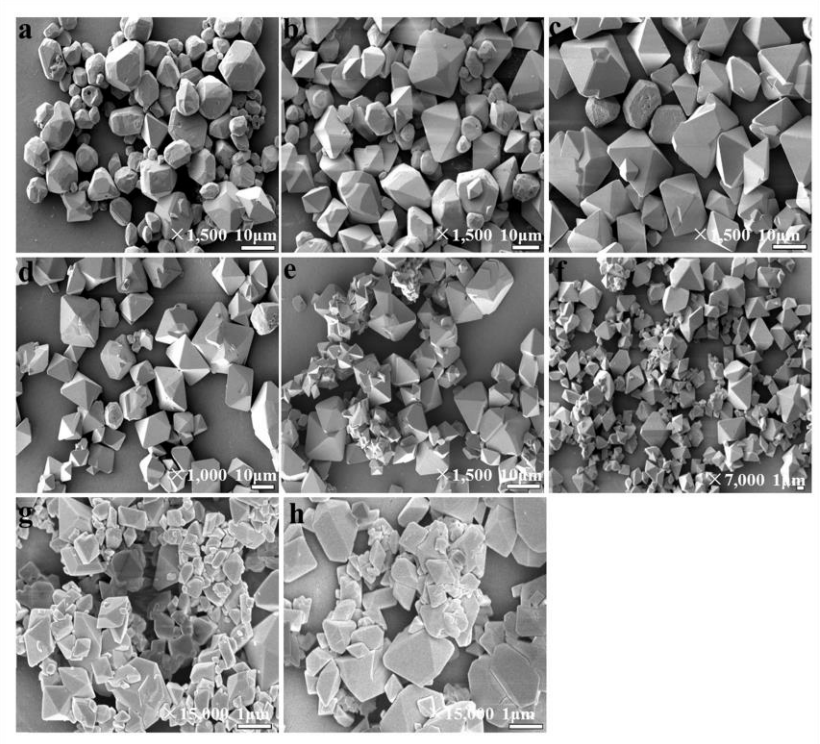

Fig. 3 SEM images of YF_3: xEu^{3+}, 1.0%Bi^{3+} (x = 0-0.175) samples prepared at V_{HNO_3} = 11 mL: (a) x = 0; (b) x = 0.025; (c) x = 0.05; (d) x = 0.075; (e) x = 0.1; (f) x = 0.125; (g) x = 0.15; and (h) x = 0.175.

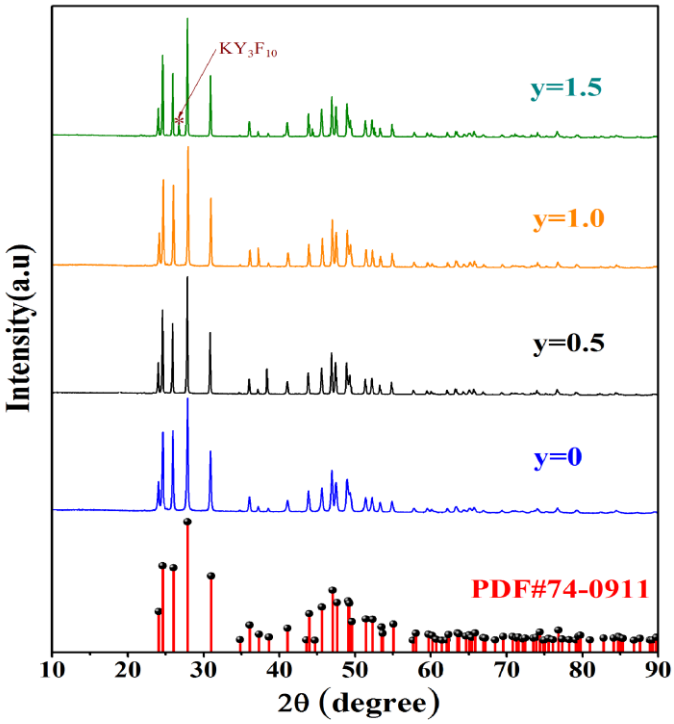

Fig. 4 XRD patterns of YF_3: $0.125Eu^{3+}$, y%Bi^{3+} samples (y = 0, 0.5, 1.0 and 1.5) prepared at V_{HNO_3} = 11mL.

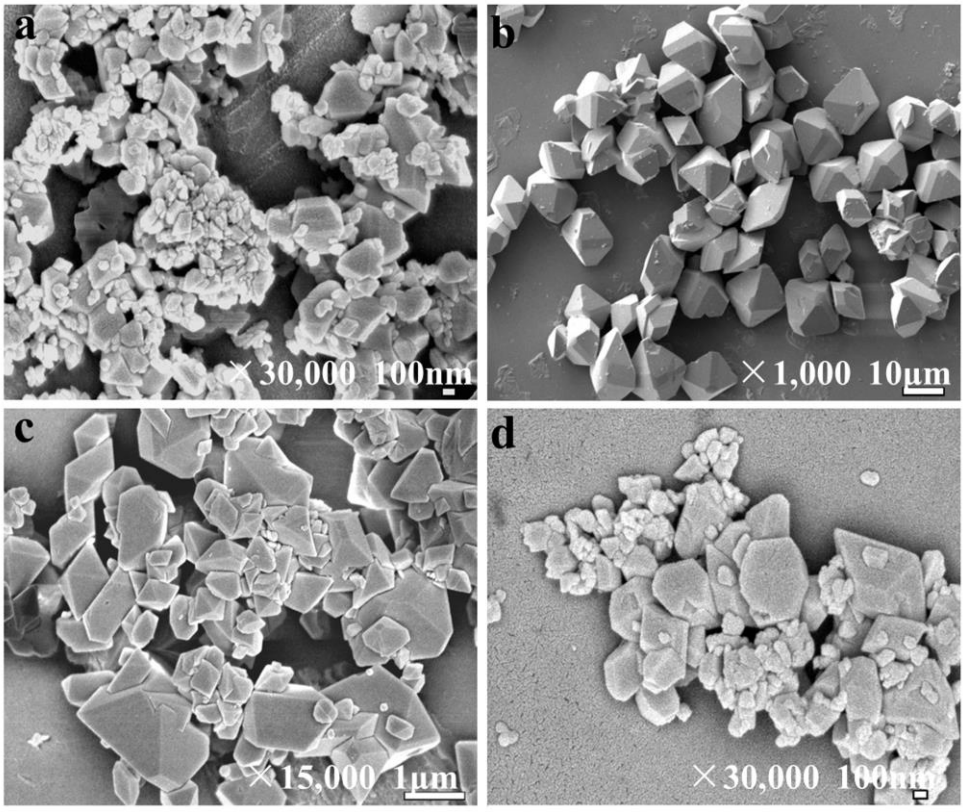

Fig. 5 SEM images of YF_3: $0.125Eu^{3+}$, y%Bi^{3+} samples prepared at V_{HNO_3} = 11mL: (a) y = 0.0; (b) y = 0.5; (c) y= 1.0; (d) = 1.5.

The emission spectra of YF_3: xEu^{3+}, $y\%Bi^{3+}$ (x/y = 0.125/0, x/y = 0.125/0.5 and x/y = 0/1.0) excited at 393 nm are shown in Fig. 6a. It was found that the emission spectra (575 nm) of the sample with x/y = 0/1.0 (i.e. without Eu^{3+} doping) should be attributed to the $^3P_1 \rightarrow {}^1S_0$ electrons transition of Bi^{3+}.[26] However, compared to the Eu^{3+}-doped materials, the emission of the materials with only Bi^{3+} doping is much weaker. The emission spectrum of the sample with x/y = 0.125/0 consists of some peaks corresponding to $^5D_1$-$^7F_0$, $^5D_1$-$^7F_2$ (515 nm and 555 nm) and $^5D_0$-^7F_J (J = 0-4; 580, 592, 614, 650, and 690 nm) electrons transition of Eu^{3+} ions, respectively.[27,28] The emission of $^5D_0$-$^7F_1$ is the strongest because of the magnetic–dipole mechanism and inversion symmetry position of Eu^{3+} ions. Interestingly, the position and shape of the peaks for the materials with x/y = 0.125/0 and 0/1.0 are almost the same, indicating that Bi^{3+} and Eu^{3+} have some parallel levels. With the addition of Bi^{3+} (y = 0.5), the emission intensity of the powders at 575 nm and 625 nm is significantly enhanced. These show that Bi^{3+} can sensitize Eu^{3+} [29] because the emission spectra of Bi^{3+} and Eu^{3+} have a significant overlap, and the interaction between Bi^{3+} and Eu^{3+} leads to the considerable enhancement in the fluorescence of the materials. Moreover, Eu^{3+} and Bi^{3+} can be simultaneously excited under ~393nm due to certain matched energy levels. Hence, the activated Bi^{3+} electrons jump to their higher energy levels $^5L_6$ and $^2P_{3/2}$, respectively.[24] Then, Bi^{3+} ions transfer the energy to the Eu^{3+} ions that have similar energy through relaxation or non-radiation.

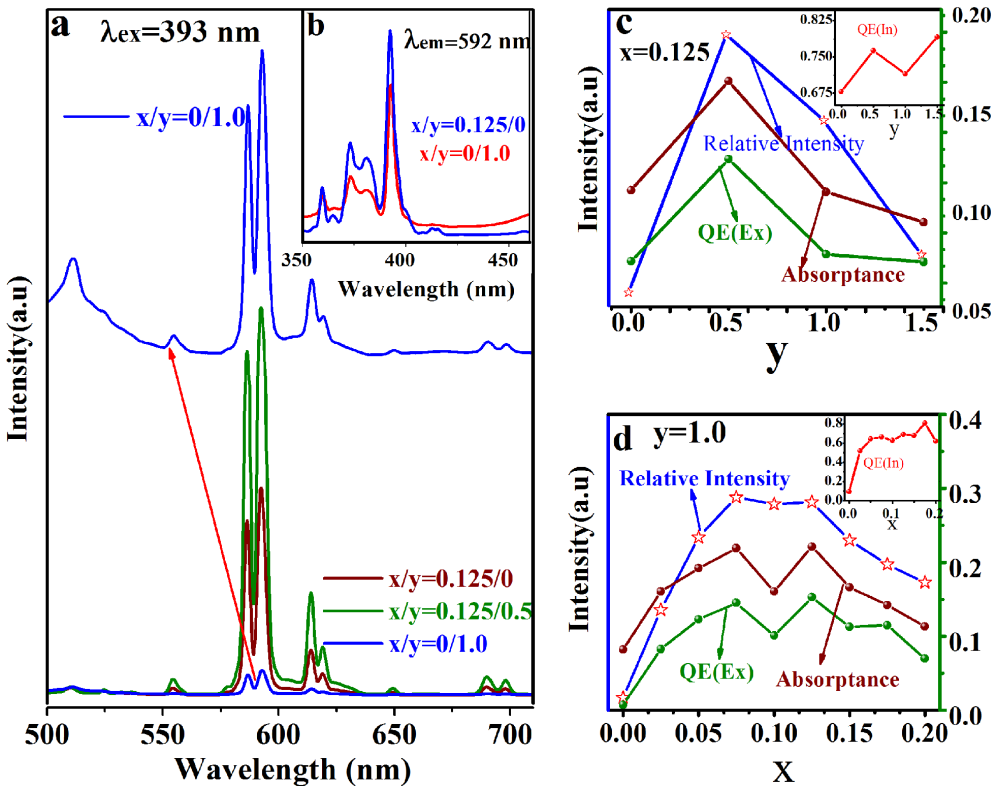

Fig. 6 (a) Emission spectra of YF_3: xEu^{3+}, $y\%Bi^{3+}$ (x = 0.125, y = 0; x = 0.125, y = 0.5; x = 0, y = 1.0) samples prepared at V_{HNO_3} = 11 mL excited at 393 nm; (b) Excitation spectra of YF_3: xEu^{3+}, $y\%Bi^{3+}$ (x = 0, y = 1.0; x = 0.125, y = 0) and λ_{em} = 592 nm; (c) and (d) Dependences of the emission intensity (λ_{em} = 592 nm), (Ex/In) quantum efficiency and absorbance on y and x.

The doping of Bi^{3+} does not change the position of emission peaks since the 4f energy level of Eu^{3+} is hardly affected by the crystal field due to the shielding effect of the $5s^2p^6$ electrons.[30] Fig 6b shows that the shape and position of excitation peaks of the YF_3: xEu^{3+}, $y\%Bi^{3+}$ with x/y = 0/1.0 and 0.125/0 have no significant difference, indicating that Bi^{3+} and Eu^{3+} have some matched energy level.

The dependences of emission intensity, external/internal quantum efficiency (QE-Ex/In) and absorbance on y and x for YF_3: $0.125Eu^{3+}$, $y\%Bi^{3+}$ and YF_3: xEu^{3+}, $1.0\%Bi^{3+}$ are shown in Figs. 6c and 6d, respectively. The results show that the emission intensity initially increases and then decreases with increasing Eu^{3+} and Bi^{3+} and the strongest fluorescence intensities of the materials

are reached at x = 0.125 and y = 0.5, respectively. Meanwhile, the external quantum (QE-Ex) and absorptance of the samples have the same tendency but the internal quantum (QE-In) shows an inconsistent trend. It can be seen that the samples possess very high internal quantum efficiency (52-81%), however, the external quantum efficiency (0.7-15%) and absorbance (8-22%) are low. The phenomenon exhibits that the materials prepared in the work have weak absorbance and need to be further improved. On the other hand, for the YF_3: xEu^{3+}, 1.0%Bi^{3+}, at low concentration of Eu^{3+}, the increasement of emission intensity with x should be attributed to the accumulating luminescent centers. In addition, the amount of H···O increases with x and the hydrogen bonding can make a stronger crystal field that applies on the Eu^{3+} ions[31,32] to enhance the fluorescent intensity of the powder. However, at high concentration of Eu^{3+}, the fluorescence of the materials decreases with increasing x because of the aggrandizing non-radioactive energy transfer among miscellaneous Eu^{3+} until reaching its quenching point; moreover, the degree of Eu^{3+}-Eu^{3+} interaction is enhanced because of shorter internuclear distance of ions with increasing Eu^{3+}, which leads to non-radiative decay of the excited state. These result in the fluorescence quenching in the materials with high levels of Eu^{3+}.[25] According to Dexter's energy transfer theory,[32] a typical effect of concentration quenching is induced by non-radioactive energy migration among adjacent luminescent ions. For the YF_3: 0.125Eu^{3+}, y%Bi^{3+}, at a low level of Bi^{3+}, the fluorescence intensity increases with y due to the increasing sensitizers that can transfer sufficient energy to the luminescent centers. However, excess Bi^{3+} may result in the formation of the Bi^{3+} clusters that dissipates the absorbed energy via non-radioactive transition[13] and thus degrades the emission intensity of the samples.

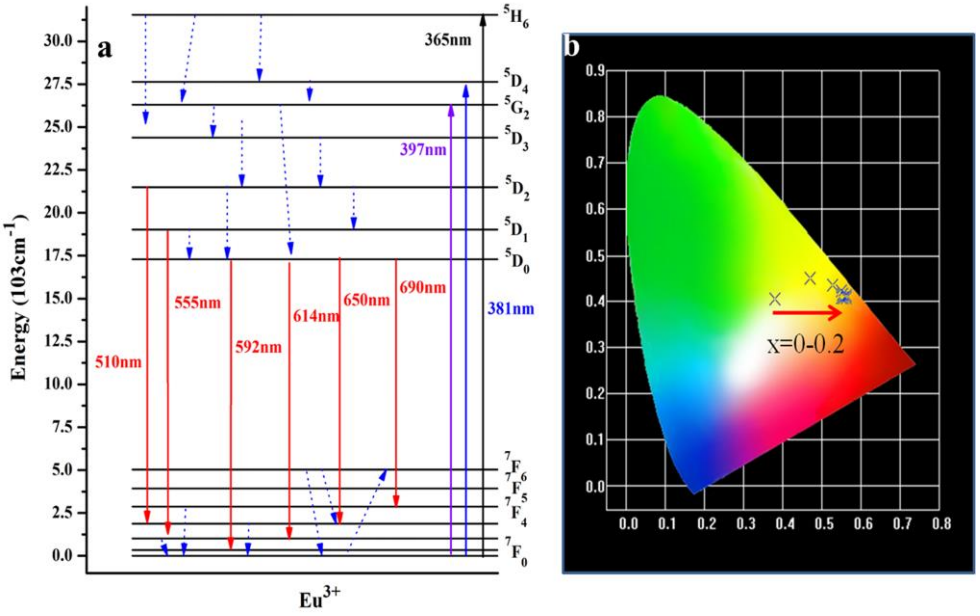

Fig. 7 (a) Schematic energy level diagram of Eu^{3+}; (b) Representation of the CIE chromaticity diagram of YF_3: xEu^{3+}, 1.0%Bi^{3+} samples (x = 0-2.0) prepared at V_{HNO_3} = 11 mL (λ_{em} = 592 nm).

The schematic energy level diagram of Eu^{3+} is shown in Fig. 7a. It intuitively reveals the electron transition process of Eu^{3+}, corresponding to the characteristic peak of emission and excitation spectra (Figs. 6a and 6b); meanwhile, it also exhibits the non-radiation transmission of energy in the materials. In general, color could be represented by the Commission International del'Eclairage (CIE) 1931 chromaticity coordinates.[33] The CIE chromaticity diagram of YF_3: xEu^{3+}, 1.0%Bi^{3+} samples with x = 0-2.0 is shown in Fig.7b. From Fig. 7b, the color of the samples is mainly in the yellow area, indicating that the Eu^{3+} ions are located in low symmetry lattices.[34] The color tone can be tuned at $x < 0.075$, and the chromaticity coordinates do not further shift when $x \geq 0.075$, indicating that the color of the optical materials strongly depends on the crystal structure. These results are consistent with XRD patterns (Fig. 1).

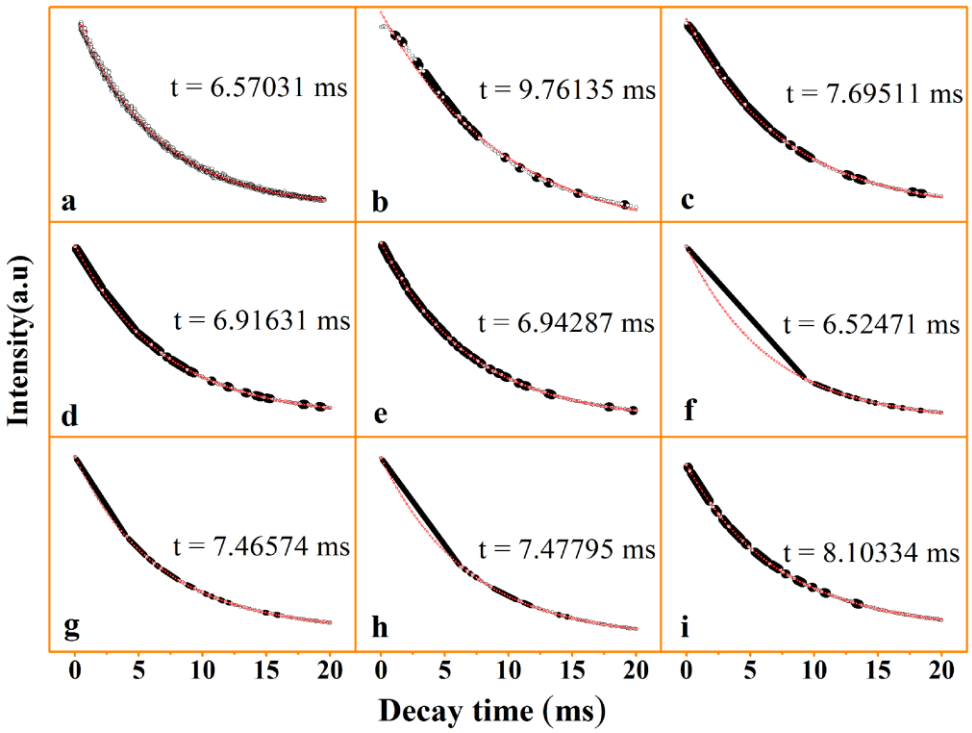

Fig. 8 Lifetime decay curves of the YF_3: xEu^{3+}, 1.0%Bi^{3+} samples prepared at V_{HNO_3} = 11 mL (the red line is fitted curve): (a) x = 0; (b) x = 0.025; (c) x = 0.05; (d) x = 0.075; (e) x = 0.1; (f) x = 0.125; (g) x = 0.15; (h) x = 0.175; and (i) x = 0.2. (λ_{ex} = 393 nm, λ_{em} = 592 nm).

The decay curves for $^5D_0$-$^7F_1$ (592 nm) of YF_3: xEu^{3+}, 1.0%Bi^{3+} with x = 0-0.2 were measured under the excitation of 393 nm at room temperature as shown in Fig. 8. The decay curve of the sample with x = 0 cannot be fitted into functions well. However, the decay curves of the powder with x = 0.025-0.15 and x = 0.175-0.20 can be well fitted by double exponential and triple exponential functions (formulas 1 and 2) as following, respectively:

$$I(t) = I_0 + A_1 \exp(-t/t_1) + A_2 \exp(-t/t_2) \quad (1)$$

$$I(t) = I_0 + A_1 \exp(-t/t_1) + A_2 \exp(-t/t_2) + A_3 \exp(-t/t_3) \quad (2)$$

where $I(t)$ and I_0 are the luminescence intensities at times of t and 0, t is the time, t_1 and t_2 are the decay times for exponential components, respectively. The average decay lifetime t can be calculated by the formulas as following:

$$t = \left(A_1 t_1^2 + A_2 t_2^2\right) / \left(A_1 t_1 + A_2 t_2\right) \quad (3)$$

and

$$t = \left(A_1 t_1^2 + A_2 t_2^2 + A_3 t_3^2 \right) / \left(A_1 t_1 + A_2 t_2 \right) \quad (4)$$

The average lifetime values of the samples with x = 0, 0.025, 0.05, 0.075, 0.01, 0.125, 0.15, 0.175 and 0.2 are calculated to be 6.57, 9.761, 7.695, 6.916, 6.942, 6.524, 7.466, 7.478 and 8.103 ms, respectively. The decay behaviors of the YF_3: $0.125Eu^{3+}$, y%Bi^{3+} samples are shown in Fig. 9. The curve of the sample with y = 0 can be fitted into bi-exponential as formula (1) and the others can be fitted into a tri-exponential well as formula (2). The average lifetime values of the samples with y = 0, 0.5, 1.0, and 1.5 are 8.899, 7.082, 7.680, 8.548 ms, respectively.

The fitting parameters of the decay time for the materials are given in Table 1. The sample with x/y = 0/1.0 has a relatively short lifetime which may be ascribed to overmuch surface defects. In general, the crystalline defect results in the formation of quenching center, which leads to non-radioactive relaxation of photons. From Table 1, some values of t_1, t_2 and t_3 of the samples with x = 0.15-0.2 and y = 0-1.5 are not identical, implying that the lattice environments of Eu^{3+} ions are not identical. The Eu^{3+} ions with a short decay time may exist near the defects and grain surfaces, whereas the Eu^{3+} ions with long decay lifetime may exist at the core of the grains with a perfect lattice environment.[35] It can be seen that the average decay time exhibits an unusual change: the optimal level of Eu^{3+} for fluorescence possesses shorter decay time than other compositions. This result does not agree with most of reports in literatures[7,15,36] in which the materials with the strongest fluorescence exhibit the longest decay time. However, Li *et al.* also reported similar unusual phenomenon.[11,33] It is well known that the number of luminescent centers, defects, energy transfer and impurities in the host material have inevitable effects on the decay of kinetic behavior of the materials.[22] Meanwhile, the morphology, edges, apexes, and special junctions of crystal grains also have important effects on the decay properties.[7] Therefore, it can be inferred that the

unusual phenomenon shown in Tab. 1 should be the end product of all these factors. However, the exact reason of the phenomenon is still not clear that needs to be further studied.

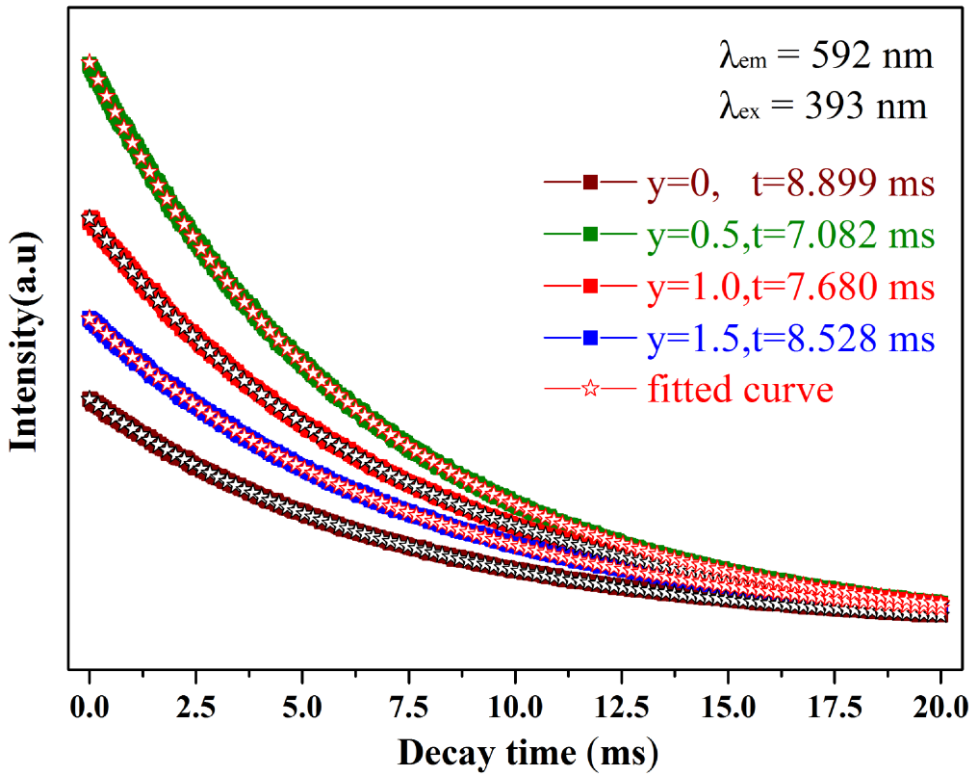

Fig. 9 Lifetime decay curves of the YF_3: $0.125Eu^{3+}$, y%Bi^{3+} samples (y = 0, 0.5, 1.0, and 1.5) prepared at V_{HNO_3} = 11 mL (λ_{ex} = 393 nm, λ_{em} = 592 nm).

Tab. 1 Fitting parameters of the decay time for YF_3: xEu^{3+}, 1.0%Bi^{3+} (x = 0-0.2) and YF_3: $0.125Eu^{3+}$, y%Bi^{3+} (y = 0-1.5)

	t_1	t_2	t_3	R^2	t_{av}
x/y = 0/1.0	6.5703	6.5703	–	0.99865	6.570
x/y = 0.025/1.0	9.7613	9.7613	–	0.99998	9.761
x/y = 0.05/1.0	7.6951	7.6951	–	0.99925	7.695
x/y = 0.075/1.0	6.9163	6.9163	–	0.99989	6.916
x/y = 0.1/1.0	6.9420	6.9420	–	0.99993	6.942
x/y = 0.125/1.0	6.5240	6.5240	–	0.99998	6.524
x/y = 0.15/1.0	10.5070	5.9808	–	0.99998	7.466
x/y = 0.175/1.0	4.1316	7.8496	7.9140	0.99995	7.478
x/y = 0.2/1.0	8.8045	4.7397	8.7968	0.99996	8.103
x/y = 0.125/0	11.6710	6.2953	–	0.99987	8.899
x/y = 0.125/0.5	9.0759	6.1508	6.1484	0.99995	7.082
x/y = 0.125/1.0	8.3245	8.3841	5.8398	0.99993	7.680
x/y = 0.125/1.5	6.9973	6.9973	11.2800	0.99990	8.528

As mentioned above, the morphology and structure of the grains can be regulated by optimizing the concentrations of Eu^{3+} and Bi^{3+} ions and the fluorescence of the samples strongly depends on the morphology of the crystals. We have noted that the concentration of H^+ (*i.e.* acidity) plays an important role in regulating the phase structure and morphology of the materials. For example, Shao *et al.* reported that the shape of crystal grain is transformed from dimond-like to octahedral-formation with the amount of HNO_3 increasing;[7] and Zhao *et al.* found that PH value affects the size and morphology of CaF_2: Yb^{3+}/Er^{3+}.[37] Obviously, as compared to optimizing chemical compositions, regulating the morphology by adjusting the amount of H^+ is much simpler and more practicable. In this work, we have successfully obtained the desired micro-topography, pure phase structure and the significant enhancement in the fluorescence of the YF_3: $0.125Eu^{3+}$, $0.5\%Bi^{3+}$ by changing the amount of HNO_3 (*i.e.* H^+).

The XRD patterns of the YF_3: $0.125Eu^{3+}$, $0.5\%Bi^{3+}$ prepared at different volume of HNO_3 are shown in Fig. 10. From Fig. 10, the precipitation is crystallized into the mixture of hexagonal KYF_4 (JCPDS No. 270466) and tetragonal KY_3F_{10} (JCPDS No. 270465) at V_{HNO_3} = 5mL. When the nitric acid is increased to 7mL, the samples are shown to be made of a large amount of KY_3F_{10} and a small amount of KYF_4 and YF_3 (JCPDS No. 740911). However, as the amount of HNO_3 reaches 11mL, all powders are transformed into pure orthorhombic YF_3 without any other impurities. In turbulent and boiling hydrothermal environment, it may exist the following reactions:

$$n\,F^- + K^+ + Y^{3+} \leftrightharpoons KY_3F_{10} / (3KYF_4) \quad (5)$$

$$H^+ + F^- \leftrightharpoons HF \quad (6)$$

$$KY_3F_{10} / (3KYF_4) + H^+ \leftrightharpoons K^+ + HF + 3YF_3 \quad (7)$$

At a low level of H^+, the excess F^- ions are coupled with cations to form multiple-fluoride (i.e., KY_3F_{10} / $3KYF_4$) as shown in formula (5). With increasing the amount of HNO_3, the H^+ ions reduce

the excess amount of F^- ions by a reversible formula (6). Finally, the excess H^+ ions can transfer the multiple-fluoride to ternary-fluoride as shown in formula (7).These mechanisms are in favor of forming the stable YF_3 phase at high volume of HNO_3.

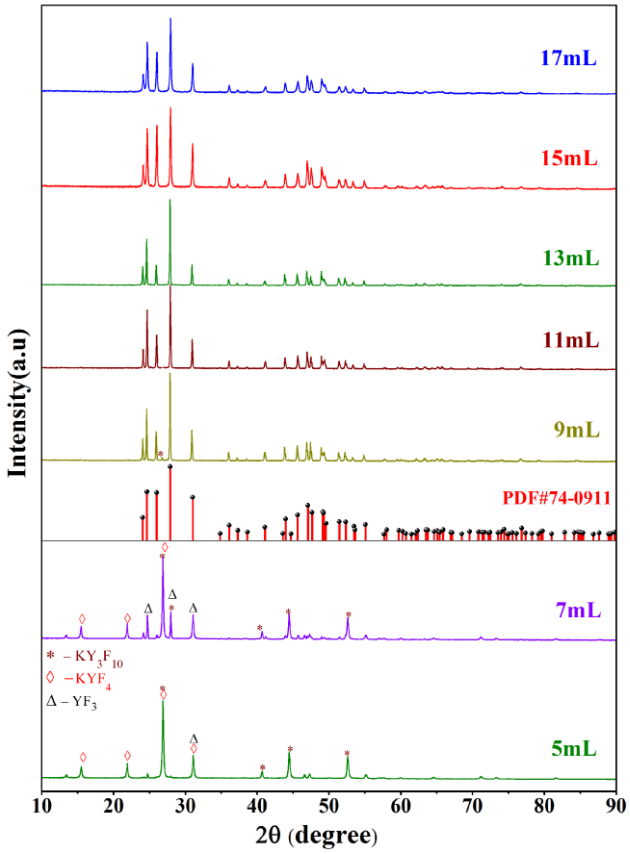

Fig. 10 XRD patterns of the YF_3: $0.125Eu^{3+}$, $0.5\%Bi^{3+}$ samples prepared at different volume of hydrogen nitrate (V_{HNO_3} = 5, 7, 9, 11, 13, 15 and 17 mL).

The morphology evolution of the YF_3: $0.125Eu^{3+}$, $0.5\%Bi^{3+}$ at different V_{HNO_3} is schematically illustrated in Fig. 11. After the addition of HNO_3, the micro-topography of YF_3: $0.125Eu^{3+}$, $0.5\%Bi^{3+}$ is obviously changed. As the amount of HNO_3 increases, the size of the samples initially increases and then decreases. From Figs. 11a-b, the samples exhibit aggregated spherical nano-particles at $V_{HNO_3} \leq 7$mL. As the amount of HNO_3 increases to 9-11mL, the crystalline grains are evolved into smooth octahedra with truncated edges and corners. It can be seen that the perfect and smooth octahedras are obtained at V_{HNO_3} = 13mL (Fig.11e). After the addition of excess HNO_3,

the diameter of the grains decrease rapidly and the larger truncated and non-truncated octahedra act as crystallization centers like nucleation as shown in Figs 11f and 11g. From the view of crystal growth, the crystalline shape of the grains highly depends on the surface energy of various crystal planes. The plane with higher surface energy grows faster than the plane with lower surface energy, so the planes with lower surface energy will be exposed.[38] From Fig. 11, it can be inferred that the surface energy of different crystal planes has been changed with increasing the amount of HNO_3. In addition, the morphology evolution of the crystal grains may be also ascribed to the decrease in the amount of the dissociative F^- with increasing HNO_3 due to the formation of HF ($H^+ + F^- \leftrightharpoons HF$) at excess H^+. It can be concluded that the morphology of the crystal grains can be effectively tuned via controlling the concentration of H^+. The relevant structures of the crystal are inserted in Fig.11 to intuitively show the evolution of crystal structure with increasing HNO_3.

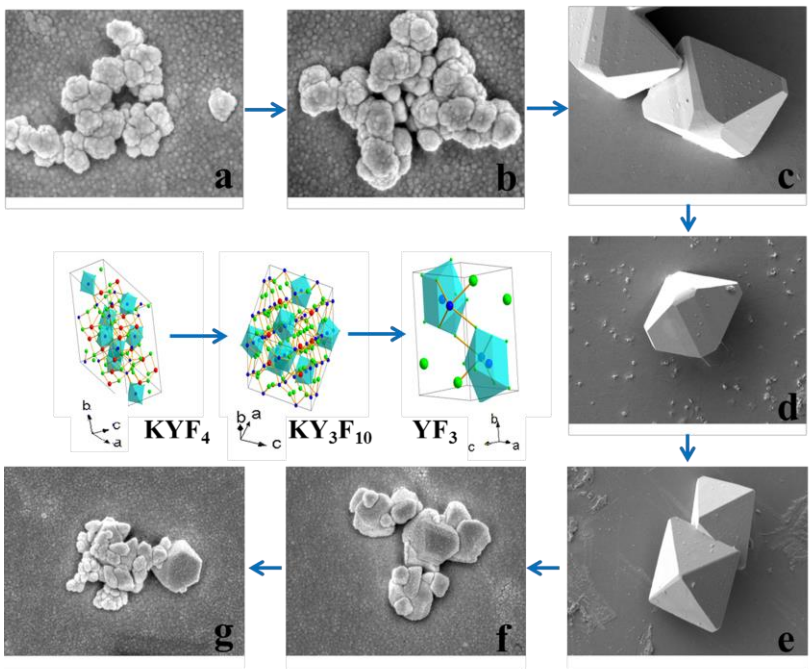

Fig. 11 Schematic illustration of the formation and morphology evolution of YF_3: $0.125Eu^{3+}$, $0.5\%Bi^{3+}$ samples prepared under different acidic conditions. (a: 5 mL, b: 7 mL, c: 9 mL, d: 11 mL, e: 13 mL, f: 15 mL, g: 17 mL)

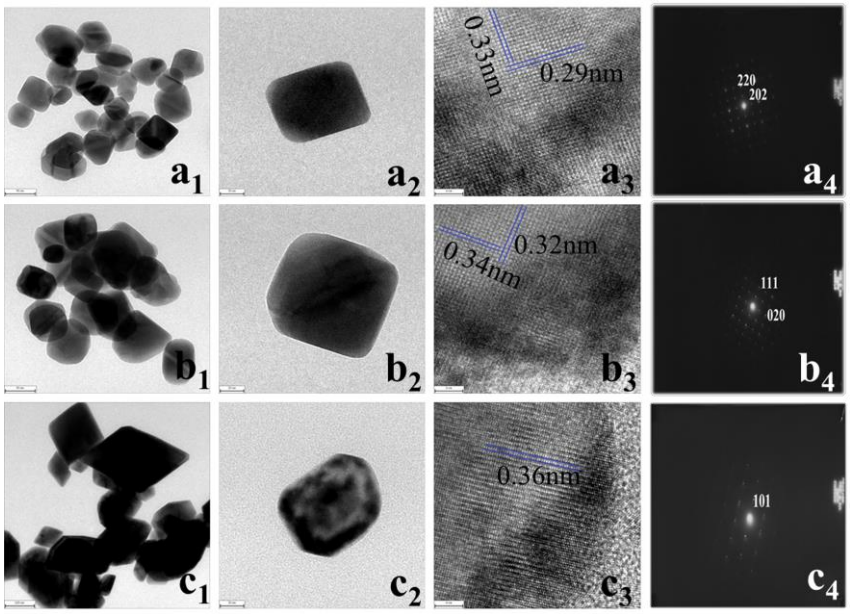

Fig. 12 TEM, HRTEM and selected area electron diffraction (SAED) images of the synthesized YF_3: $0.125Eu^{3+}$, $0.5\%Bi^{3+}$ samples prepared at 7 mL ($a_{1\text{-}4}$); 11 mL ($b_{1\text{-}4}$) and 15 mL ($c_{1\text{-}4}$) HNO_3.

To give a careful observation and confirm the changes in morphology induced by the addition of HNO_3, TEM and corresponding selected area electron diffraction (SAED) images of the YF_3: $0.125Eu^{3+}$, $0.5\%Bi^{3+}$ samples synthesized at different V_{HNO_3} are shown in Fig. 12. From Figs. $12a_1$ and a_2, it can be clearly seen that the samples are tetragonal nanocrystals of KY_3F_{10} with uniform morphology. From the HRTEM image (Fig. $12a_3$), the high crystallinity is confirmed by the clear lattice fringes. The determined interplanar distances of 0.33 nm and 0.29 nm between the adjacent lattice planes agree well with the d_{202} and d_{220} spacing of tetragonal KY_3F_{10}, respectively. Besides, the SAED pattern in Fig. $12a_4$ can be indexed to the reflection of the tetragonal KY_3F_{10}, which is consistent with the XRD results. Figs. $12b_1$ and b_2 show TEM images of the YF_3 microcrystal prepared at V_{HNO_3} = 11mL. The sample shows a rhombic base of truncated octahedron with uniform morphology.[21] The HRTEM (Fig. $12b_3$) displays the *d*-spacing of 0.32 nm and 0.34 nm corresponding to the d_{111} and d_{020} spacing of orthorhombic phased YF_3, respectively, in accordance with the XRD patterns (Fig. 10) and the SAED (Fig. $12b_4$). With increasing the amount of HNO_3,

the nanoparticles exhibit nonuniform morphology as shown in Fig. 12c$_1$. The interplanar distance is 0.36 nm, which indexes to the (101) plane of the orthorhombic YF_3. These results make a clear indication that the amount of H^+ plays a significant role in tuning the morphology and phase structure of the materials.

The emission spectra (monitored at 393 nm) of the YF_3: 0.125Eu^{3+}, 0.5%Bi^{3+} samples synthesized at V_{HNO_3} = 5-17 mL are shown in Fig. 13a, while the external/internal quantum efficiency(QE-Ex/In) and absorbance of the samples are shown in Fig.13b. The spectra exhibit a typical linear feature of Eu^{3+} emission, which display sharp peaks at the range of 550~710 nm corresponding to the electrons of Eu^{3+} transition from the excited levels ^5D_i (I = 0, 1) to ground state ^7F_j (j = 0-4) levels, respectively. As V_{HNO_3} increases, there is a slight shift at ~592nm and ~620nm of the emission peaks, indicating that the 4f energy levels of Eu^{3+} are affected due to the change in the circumstance caused by increasing hydrogen nitrate. From Fig. 13, the emission intensity at ~592nm first increases and then decreases with the amount of HNO_3 increasing, giving the strongest intensity at V_{HNO_3} = 11mL. At low level of HNO_3, the agglomerative and small particles with large surface area lead to more defects that provide non-radioactive recombination pathways,[22] resulting in the low emission intensity of the samples. The sample with V_{HNO_3} = 11mL has the strongest emission intensity due to the apparent sharp edges and corners of the crystalline grains being truncated that would decrease the non-radioactive energy transition. However, when HNO_3 is excess (V_{HNO_3} > 13mL), the size of crystal grains decreases and some small particles agglomerate on the large grains. These would increase the non-radiative energy because of larger surface area, resulting in the degradation in the fluorescence of the powder. From Fig. 13b, the (QE-Ex/In) quantum efficiency and absorbance of the samples exhibit the similar tendency.

Unfortunately, the materials have considerably low external quantum efficiency(4.7-19%) and absorbance (9-27%) in spite of their high internal quantum efficiency of 15-72%.

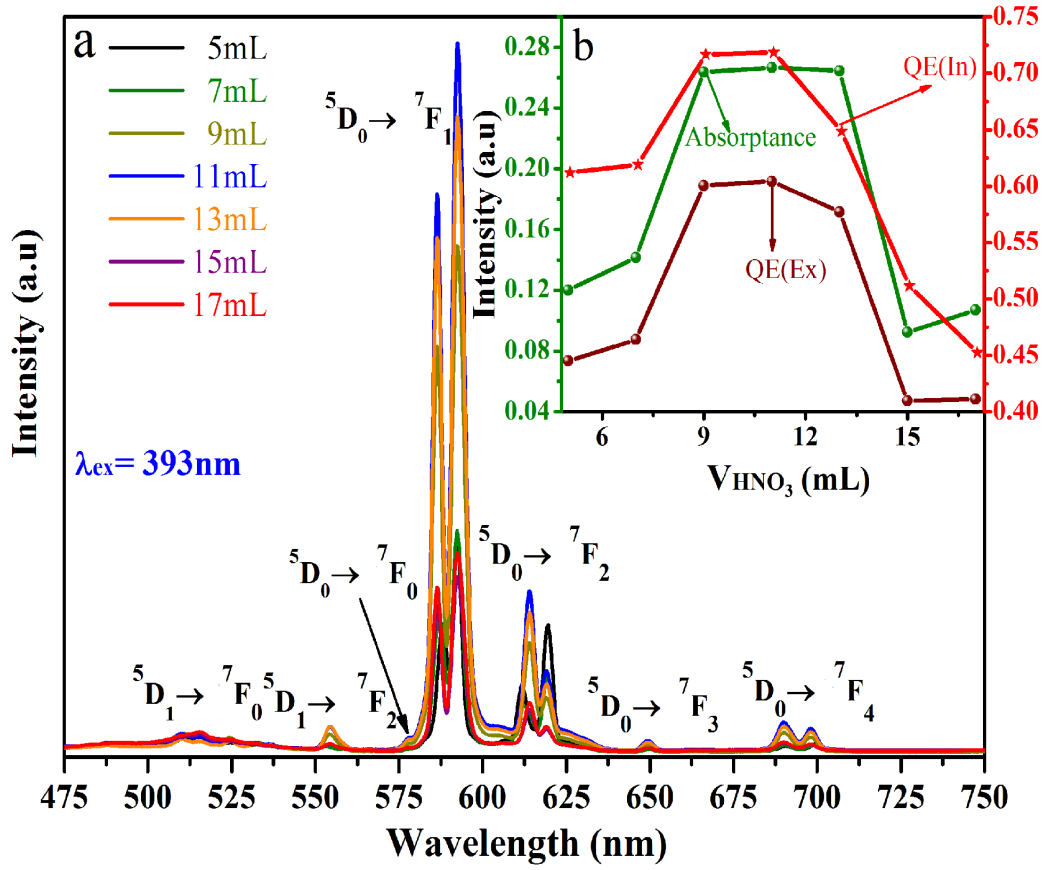

Fig. 13 (a) Emission spectra of YF_3: $0.125Eu^{3+}$, $0.5\%Bi^{3+}$ samples excited at 393 nm and obtained under different acidic conditions, (b) (Ex/In) quantum efficiency and absorbance of the samples.

Fig. 14 shows the lifetime decay curves of the YF_3: $0.125Eu^{3+}$, $0.5\%Bi^{3+}$ prepared at different V_{HNO_3}. As illustrated in Fig. 14, at $V_{HNO_3} \leq 11mL$, the decay curves emission (λ_{ex} = 393nm, λ_{em} = 592nm) for the $^5D_0$-$^7F_1$ transition of Eu^{3+} can be fitted by double-exponential (formula 1), while the decay curves of the samples with $V_{HNO_3} > 11mL$ can be fitted well with a tri-exponential (formula 2). The average values are shown in Fig. 14. The fitting results of the fluorescent lifetime of all the samples possess a desired accuracy (R^2) of 99.95-99.99%. In general, the decay life is an inverse of the sum of the non-radioactive and radioactive probabilities[15] and the fluorescent lifetime is proportional to the intensity of fluorescence. However, the present samples do not follow the rule.

As known, besides the defects of crystal grains, the morphology, edges, apexes, and special junctions of crystal particles could also have a crucial influence on the fluorescent lifetime. Therefore, it can be inferred that the present unusual phenomenon may be attributed to the comprehensive effect of the size, surface morphology, and apexes of crystalline grains.

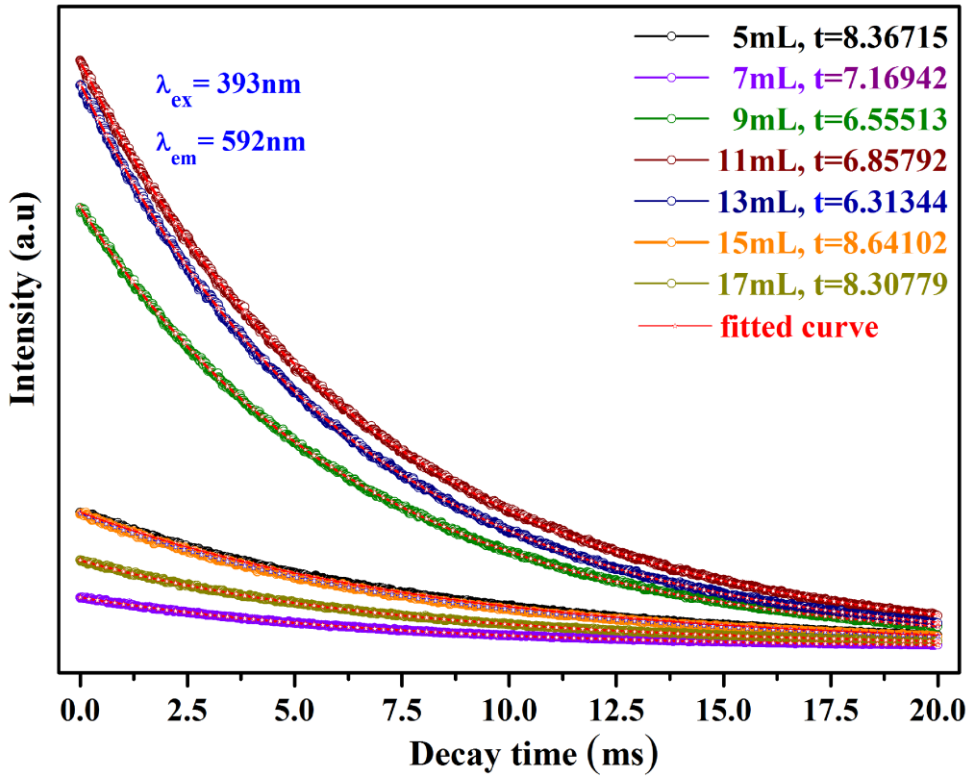

Fig. 14 Lifetime decay curves of the YF_3: $0.125Eu^{3+}$, $0.5\%Bi^{3+}$ prepared under different acidic conditions.

Conclusions

In conclusion, the powders of the YF_3: x Eu^{3+}, y% Bi^{3+} (x = 0-0.2, y = 0-1.5) have been successfully synthesized via a facile hydrothermal route. The evolutionary mechanisms of micro-topography, microstructure and crystal structure of the samples have been analyzed in detail, and the fluorescent and decay properties of YF_3: xEu^{3+}, $y\%Bi^{3+}$ have been discussed systematically. The results indicate that the concentrations of Eu^{3+}, Bi^{3+} and HNO_3 are responsible for the shape and phase structure of samples. The emission intensity of the samples is greatly enhanced by Bi^{3+}

doping because Bi^{3+} acts as an effective sensitizer so as to transfer the energy to Eu^{3+}. The optimal concentration of $Eu^{3+}$and Bi^{3+} for fluorescence are x = 0.125 and y = 0.5, respectively. The desired morphology of YF_3: 0.125 Eu^{3+}, 0.5%Bi^{3+} with excellent fluorescence has been obtained via optimizing the amount of HNO_3 and the optimal volume of HNO_3 is 11 mL. The YF_3 possesses a typical orthorhombic phase and the samples with regular truncated octahedral micro-topography exhibit the strongest emission, suggesting that the fluorescent properties of the material are strongly related to the size and morphology of the crystal grains. The present study suggests a simple method to regulate the morphology and phase structure to improve the fluorescent properties of the materials.

Acknowledgments

This work was supported by the projects of Education Department of Sichuan Province (15ZA0037 and 15ZB0032)

References

1 Z. Q. Li, C. L. Li, Y. Y. Mei, L. M. Wang, G. H. Du and Y. J. Xiong, *Nanoscale*., 2013, **5**, 3030-3036.

2 C. X. Li and J. Lin, *J. Mater. Chem*., 2010, **20,** 6831-6847.

3 X. Wang, J. Zhuang, Q. Peng and Y. D. Li, *Inorg. Chem.*, 2006, **45**, 6661-6665.

4 J. S. Wang, W. R. Miao, Y. X. Li, H. C. Yao and Z. J. Li, *Mater. Lett*., 2009, **63**, 1794-1796.

5 S. L. Zhong, S. J. Wang, H. L. Xu, C. G. Li, Y. X. Huang, S. P. Wang and R. Xu, *Mater. Lett*., 2009, **63**, 530-532.

6 C. Y. Cao, W. P. Qin, J. S. Zhang, Y. Wang, P. F. Zhu, G. F. Wang, G. D. Wei, L. L. Wang and L. Z. Jin, *J. Fluorine. Chem*., 2008, **129**, 204-209.

7 B. Q. Shao, Q. Zhao, N. Guo, Y. C. Jia, W. Z. lv, M. M. Jiao, W. Lü and H. P.You, *Cryst. Growth Des*., 2013, **13**, 3582-3587.

8 V. Caratto, F. Locardi, G. A. Costa, R. Masini, M. Fasolietc, L. Panzeri, M. Martini, E. Bottinelli, E. Gianotti and I. Miletto, *Appl. Mater. Interfaces*., 2014, **6**, 17346-17351.

9 A. Arakcheeva, D. Logvinovich, G. Chapuis, V. Morozov, S. V. Eliseeva, J-C. G. Bünzli and P. Pattison, *Chem. Sci*., 2012, **3**, 384-390.

10 G. X. Liu, X. Li, X. T. Dong and J. X. Wang, *J. Nanopart. Res*., 2011, **13**, 4025-4034.

11 D. Li, W. S. Yu, X. T. Dong, J. X. Wang and G. X. Liu, *J. Fluorine. Chem*., 2013, **145**, 70-76.

12 J. L. Blin, A. Lorriaux-Rubbens, F. Wallart and J. P. Wignacourt, *J. Mater. Chem*., 1996, **6**, 385-389.

13 G. Y. Dong, C. C. Hou, Z. P. Yang, P. F. Liu, C. Wang, F. C. Lu and X. Li, *Ceram. Int*., 2014, **40**, 14787-14792.

14 Z. L. Fu, X. Y. Cui, S. B. Cui, X. D. Qi, S. H. Zhou, S. Y. Zhang and J. H. Jeong, *CrystEngComm.*, 2012, **14**, 3915-3922.

15 L. L. Wang, Q. L.Wang, X. Y.Xu, J. Z. Li, L. B. Gao, W. K. Kang, J. S. Shi and J. Wang, *J. Mater. Chem*., 2013**, 1**, 8033-8040.

16 M. Y. Ding, S. L. Yin, D. Q. Chen, J. S. Zhong, Y. R. Ni , C. H. Lu, Z. Z. Xu and Z. G. Ji, *Appl. Surf. Sci*., 2015, **333**, 23-33.

17 Z. L. Wang, J. H. Hao, H. L. W. Chan, W. T. Wong and K. L. Wong, *Small*., 2012, **8**, 1863-1868.

18 Z. H. Xu, Y. Gao, X. Ge and Y. G. Sun, *Chem. Res. Chin. Univ*., 2013, **29**, 1-5.

19 A. Whiteside, C. A. J. Fisher, S. C. Parker and M. S. Islam, *Phys. Chem. Chem. Phys*., 2014**,** **16**, 21788-21794.

20 J. L. Lemyre and A. M. Ritcey, *Chem. Mater*., 2005, **17**, 3040-3043.

21 F. Tao, Z. J. Wang, L. Z. Yao, W. L. Cai and X.G. Li, *Cryst. Growth. Des*., 2007, **7**, 854-858.

22 Y. C. Chen, C. C. Wu, D.Y. Wang and T. M. Chen, *J. Mater. Chem*., 2012, **22**, 7961-7969.

23 D. G. Truhlar, W. L. Hase and J. T. Hynes, *J. Phys. Chem*., 1983, **87**, 2664-2682.

24 S. P. Singh and B. Karmakar, *RSC Adv*., 2011, **1**, 751-754.

25 B. S. Naidu, B. Vishwanadh, V. Sudarsan and R. K. Vatsa, R. *Dalton. Trans*., 2012**,** **41**, 3194-203.

26 L. Chen, K. J. Chen, S. F. Hu and R. S. Liu, *J. Mater. Chem*., 2011, **21**, 3677-3685.

27. M. Ajmal and T. S. Atabaev, *Opt. Mater*., 2013,**35**,1288-1292.

28. G. G. Li, Y. J. Liang, M. F. Zhang and D. Y. Yu, *CrystEngComm*., 2014,**16**,6670-6679.

29 A. Escudero, E. Moretti and M. Ocaña, *CrystEngComm*., 2014, **16**, 3274-3283.

30 C. Gong, Q. J. Li, R. Liu, Y. Hou, J. X. Wang, X. T. Dong, B. Liu, X. Yang, Z. Yao, X. Tan, D. M. Li, J. Liu, Z. Q. Chen, B. Zou, T. Cui and B. B. Liu, *Phys. Chem. Chem. Phys*., 2013, **15**, 19925-19931.

31 P. Ghosh and A. Patra, *J. Phys. Chem. C*., 2008**, 112**, 3223-3231.

32 F. W. Kang, M. Y. Peng, X. B.Yang, G. P. Dong, G. C. Nie, W. J. Liang, S. H. Xu and J. R. Qiu, *J. Mater. Chem*., 2014**, 2**, 6068-6076.

33 D. Li, J. X. Wang, X. T. Dong, W. S. Yu and G. X. Liu, *J. Mater. Sci*., 2013**, 48**, 5930-5937.

34 V. Sudarsan , F. C. J. M. Van Veggel, R. A. Herring and M. Raudsepp, *J. Mater. Chem.*, 2005, **15**, 1332-1342.

35 A. K. Parchur and R. S. Ningthoujam, *RSC Adv*., 2012, **2**, 10859-10868.

36 A. Gnach and A. Bednarkiewicz, *Nano. Today*., 2012**, 7**, 532-563.

37 J. Zhao, Y. J. Zhu, J. Wu and F. Chen, *J. Colloid. Interface. Sci*., 2015, **440**, 39-45.

38 B. J. Wileny, T. S. Herricks, Y. G. Sun and Y. N. Xia, *Nano. Lett*., 2004, **4**, 1733-1739.